ELSEVIER

Contents lists available at ScienceDirect

Earth and Planetary Science Letters

journal homepage: www.elsevier.com/locate/epsl



North China as a mechanical bridge linking Pacific subduction and extrusion of the Tibetan Plateau



Fengming Shen^a, Lifeng Wang^{a,b,c,*}, Sylvain Barbot^d, Jiahong Xu^e

- ^a State Key Laboratory of Earthquake Dynamics, Institute of Geology, China Earthquake Administration, Beijing, China
- ^b Shanxi Taiyuan Continental Rift Dynamics National Observation and Research Station, Beijing, China
- ^c Jilin Changbaishan Volcano National Observation and Research Station, Beijing, China
- ^d Department of Earth Sciences, University of Southern California, Los Angeles, USA
- e State Key Laboratory of Earth Surface Processes and Resource Ecology, Faculty of Geographical Science, Beijing Normal University, Beijing, China

ARTICLE INFO

Article history: Received 2 June 2023 Received in revised form 13 August 2023 Accepted 14 September 2023 Available online 5 October 2023 Editor: J.-P. Avouac

Keywords: GNSS North China mechanical bridge kinematics

ABSTRACT

North China, one of the most populated regions in the world, is exposed to elevated seismic hazards and has experienced multiple $M \geq 8$ earthquakes in the past 1,000 years. The recent 1976 Ms 7.8 Tangshan earthquake constitutes a vivid reminder of the tectonic activity. Yet, the tectonic origin of the regional seismic unrest remains poorly understood. Here, we use geodetic data to construct a kinematic model encompassing the North China Block (NCB) and its neighboring Amurian Block (AB) and the South China Block (SCB) to illuminate the link between lithospheric strain accumulation and seismic activity. Our analysis illuminates two east-west oriented left-lateral shear zones that decouple the AB from the NCB, the latter representing a collage of the North China Plain (NCP) and the Ordos Block (OB). Bookshelf faulting slices the NCP through a series of NNE-trending right-lateral and conjugate WNW-trending left-lateral shear zones. These shear zones drive historical and instrumental seismic activities. The NCB serves as a mechanical bridge accommodating the relative motion of the surrounding mobile tectonic units. In the far field, Pacific subduction at the Japan Trench, extrusion of the Tibetan plateau, and retreat at the Ryukyu trench cause internal strain within the NCB, leading to the frequent occurrences of destructive earthquakes.

© 2023 Elsevier B.V. All rights reserved.

1. Introduction

North China hosts a large population and numerous economic hubs. Wedged between the Amurian Block (AB) and the South China Block (SCB), the North China Block (NCB) represents a collage of the North China Plain (NCP) and the Ordos Block (OB), and experiences internal deformation (e.g., Y. Zhang et al., 2003; Wang and Shen, 2020) that results in considerable seismic hazards (Fig. 1). Within the past 1,000 years, multiple $M \geq 8$ earthquakes have caused numerous casualties and economic loss (Bolt, 1985). The most recent 1976 Tangshan earthquake alone, with a surface wave magnitude (Ms) of 7.8, caused 240,000 deaths. As the population and infrastructure have exploded since then, it is important to refine our understanding of tectonic processes in North China.

E-mail addresses: wanglf@ies.ac.cn, chsxwlf@hotmail.com (L. Wang).

The tectonic history and active fault zones in North China have been extensively explored (e.g., Xu et al., 1993; Zhu et al., 2015, 2017; Guo and Zhao, 2019), but the causes of frequent destructive earthquakes on active fault zones traversing the NCP remain elusive (Fig. 1). A possible rationale for the occurrence of large earthquakes in NCP is bookshelf faulting of a series of NNE-trending dextral faults accommodating the sinistral motion between the AB and the SCB (Zhang et al., 2018), reminiscent of the kinematics of right-lateral faults in the Mojave section of the Eastern California Shear Zone (Garfunkel, 1974). Yet, the role of these structures in the broader tectonic context is still unknown. This study aims to shed new light on the internal deformation of the NCB in the context of the large-scale kinematics of Eastern China.

Tectonic geodesy has become a powerful tool to constrain contemporary crustal deformation (Thatcher, 2009; Avouac, 2015; Elliott et al., 2016), but the application of classical geodetic techniques is challenging in Eastern China due to small crustal deformation and the sparseness of GNSS stations in the past. Previous studies resolved little relative motion between the tectonic blocks (e.g., Shen et al., 2000; He et al., 2003) and could hardly reconcile the detected internal strain with the seismic activity within the

^{*} Corresponding author at: State Key Laboratory of Earthquake Dynamics, Institute of Geology, China Earthquake Administration, Beijing, China.

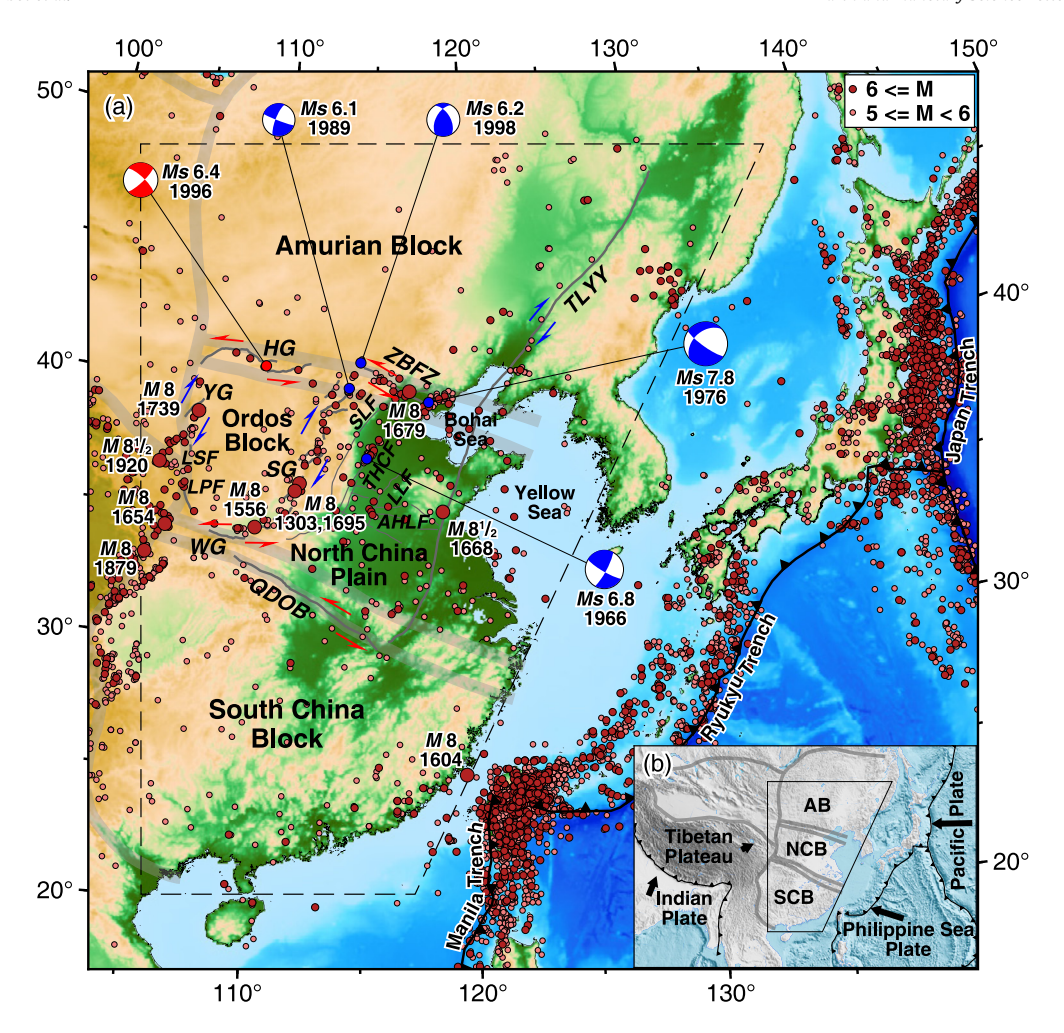


Fig. 1. Tectonic setting of Eastern China. (a) Eastern China represents an amalgamation of several tectonic units, outlined by thick gray lines (P. Zhang et al., 2003): the Amurian Block (AB), the North China Block (NCB, a collage of the North China Plain, NCP and the Ordos Block, OB), and the South China Block (SCB). The major fault zones (thin lines) are mostly located in or around the NCB, including the Tancheng-Lujiang-Yilan-Yitong fault zone (TLYY), Qinling-Dabie Orogenic belt (QDOB), Zhangjiakou-Bohai fault zone (ZBFZ), Hetao Graben (HG), Shanxi Graben (SG), Weihe Graben (WG), Yinchuan Graben (YG), Luoshan fault zone (LSF), and Liupanshan fault zone (LFP). Active fault zones within the NCP include the Anyang-Heze-Linyi fault zone (AHLF), Sanhe-Laishui fault zone (SLF), Tangshan-Hejian-Cixian Fault zone (THCF), and Liaocheng-Lankao fault zone (LLF). The red and pink dots are the historical $M \ge 5$ earthquakes from 1831 BC to 1969 AD (Bolt, 1985) and $Ms \ge 5.0$ earthquakes since 1970 (from China Earthquake Networks Center, National Earthquake Data Center, http://data.earthquake.cn); the historical $M \ge 8$ earthquakes are labeled. The instrumental $Ms \ge 6.0$ earthquakes are shown with red and blue-filled beach balls, respectively for sinistral and dextral dislocation. (b) Eastern China in a broader tectonic context.

NCB (Zheng et al., 2017; Wang and Shen, 2020). Here, we use the most recent compilation of geodetic observations in Eastern China, allowing us to detect previously unrecognized deformation. Using these data, we constrain a kinematic model that incorporates slip on major faults and distributed deformation in the lower crust. As the vertical observation is only accessible at a few scattered stations and the dataset contains large uncertainties (e.g., Pan et al., 2021), we focus on the distribution of horizontal shear, which can be constrained well.

The paper is structured as follows. We first introduce the geological setting of Eastern China. Then, we describe the kinematic modeling approach in Section 3 and the compilation of geodetic data in Section 4. The modeling results are presented in Section 5. We discuss the internal deformation of Eastern China in the context of plate tectonics and seismicity in Section 6. Our results indicate that the NCB fills the space problem posed by subduction of the Pacific plate underneath the AB (Zhu and Xu, 2019), retreat of the Philippine Sea plate under the Ryukyu trench (Holt et al., 2018; Liu et al., 2022), and tectonic escape of the Tibetan plateau (Royden et al., 2008). Acting as a mechanical bridge, the NCB modulates the relative motion of its neighbors in all cardinal directions, resulting in frequent occurrences of large earthquakes.

2. Geological setting of Eastern China

The continental assembly of Eastern China represents a collage of several tectonic blocks since the Archean (Zheng et al., 2013). The North China Block (NCB) has been a coherent craton since the late Archean to Paleozoic (Liu et al., 1992). The amalgamation between the western and eastern NCB, now related to the Ordos Block (OB) and North China Plain (NCP), occurred \sim 1.85 Ga (Zhao et al., 2005). The NCP participated in the destruction of the North China craton, experiencing tectonic reactivation that led to lithospheric thinning and widespread rifting during the Late Mesozoic-Cenozoic (Xu and Ji, 2015; Wu et al., 2019), forming the unstable crust of the NCP (Wang et al., 2017). During that time, the OB was less involved in this process and most likely preserves its old cratonic keel (Menzies et al., 2007). Large-scale uplift occurred in the OB, resulting in the formation of grabens (Deng et al., 1999). The suture between the Tuva-Mongolia orocline (the main part of the present Amurian Block, AB) in the North, itself the consolidation of several Precambrian to Permian subduction-accretion terranes, and the NCB possibly occurred in the late Paleozoic (Xiao et al., 2018). Extensive left-lateral fault zones (e.g., the Zhangjiakou-Bohai fault zone, ZBFZ) developed between the AB and NCB during the Cenozoic (Deng et al., 1999; Xu and Ji, 2015). The NNE-trending Tancheng-Lujiang fault and its northern branch Yilan-Yitong fault (TLYY), which separates the NCP from the Yellow Sea Basin, originated during the Triassic-Jurassic and have experienced multiple stages of deformation with alternate senses of motion since that time (Zhu et al., 2007, 2010). The NW-trending Qinling-Dabie Orogenic belt (QDOB) represents an accretionary margin between the NCB and the South China Block (SCB) that ultimately formed during the Triassic (Meng and Zhang, 1999) when the SCB rotated clockwise relative to the NCB (Zhao and Coe, 1987; Meng et al., 2005; Tan et al., 2007).

The tectonic blocks are associated with major, seismically active fault zones (P. Zhang et al., 2003) in Eastern China. The boundary between the AB and the NCB coincides with the Hetao Graben (HG) and the Zhangjiakou-Bohai fault zone (ZBFZ) (Zonenshain and Savostin, 1981; Zhang et al., 2018), which notably hosted the 1996 Ms 6.4 Baotou and 1998 Ms 6.2 Zhangbei earthquakes. The west and south borders of the OB can be identified with the seismically active Yinchuan Graben (YG), the Luoshan fault zone (LSF), the Liupanshan fault zone (LPF), and the Weihe Graben (WG). The boundary between the OB and the NCP is now collocated with the NNE-trending Shanxi Graben (SG) (Ye et al., 1987) that generated multiple M 8 earthquakes in the past 1,000 years and the recent 1989 Ms 6.1 Datong-Yanggao earthquake. The boundary between the NCB and the SCB is identified with the QDOB.

Active fault zones are also present within the NCP. The NNE-trending Sanhe-Laishui fault zone (SLF), Tangshan-Hejian-Cixian fault zone (THCF), and the NW-trending Anyang-Heze-Linyi Fault zone (AHLF) represent neotectonic structures developed from basement faults formed during the craton destruction and rifting in the Cretaceous-Paleogene, while the Liaocheng-Lankao fault zone (LLF) is a major Paleogene basement fault that remains active (Han et al., 2003; Xu and Ji, 2015). These fault zones embedded within the NCP are characterized by low spatial continuity and less maturity, and produced multiple large earthquakes, including the 1966 Ms 6.8 Xingtai and the devastating 1976 Ms 7.8 Tangshan earthquake on the THCF, the 1679 M 8 Sanhe-Pinggu earthquake on the SLF, the 1830 M $7^1/_2$ Cixian and 1937 M 7 Heze earthquake on the AHLF (Xu and Ji, 2015).

3. Kinematic modeling

We construct a kinematic model of lithospheric deformation incorporating deformation beneath the seismogenic upper crust localized along major active faults and distributed deformation in the lower crust and upper mantle that may relate to distributed deep shear zones. In this way, deformation sources originating from both brittle and ductile regimes are encapsulated (see Fig. 2). The approach generalizes the block modeling approach (Meade and Loveless, 2009), allowing the detection of previously unmapped shear zones (Barbot, 2020; Barbot and Weiss, 2021; Wang and Barbot, 2023). We do not treat the lower crust and the upper mantle separately due to the limited vertical resolution afforded by surface geodetic observations. We include the major active fault zones related to the block boundaries, i.e., TLYY, QDOB, ZBFZ, HG, SG, WG, YG, LSF, and LPF, which are presumably deep-rooted and play important roles in regional tectonics. For those grabens as well as the LSF and LPF surrounding OB, we incorporate branches that are relatively mature with well-constrained subsurface geometry (e.g., Chen and Nabelek, 1988; The Research Group, 1988; Xu et al., 1998; Min et al., 2013; Zhu et al., 2015; Wu et al., 2020). The active faults are discretized into triangular elements of \sim 75 km². We assume interseismic creep at the depths between 12 and 25 km for Eastern China, according to the depth distribution of seismicity (Fig. S1, Luo et al., 2012; Teng et al., 2014; Dong et al., 2018) and Crust 1.0 (Laske et al., 2013). For the underlying plastic substrate, we discretize the region into semi-infinite volume elements

with a dimension of $50 \times 50 \text{ km}^2$ (Fig. 2). The resulting structural model is summarized in Table S1.

In this model, the geodetic velocity can be composed of three parts: 1) aseismic fault creep beneath the seismogenic upper crust, 2) distributed deformation in the lower crust and upper mantle, and 3) overall rotation and translation that can be captured on a sphere by rotations about three orthogonal axes. The latter depends on the adopted reference frame of the geodetic data. Accordingly, the velocity field (d) can be decomposed as

$$\mathbf{d} = \mathbf{G}_e \mathbf{e} + \mathbf{G}_s \mathbf{s} + \mathbf{R} \boldsymbol{\omega},\tag{1}$$

where \mathbf{e} represents the plastic strain-rate tensors on volume elements in the lower crust and upper mantle, \mathbf{s} represents fault slip rates on surface elements beneath the seismogenic upper crust, and $\boldsymbol{\omega}$ is a vector of 3 spin rates about the rotation poles. The linear projections between the deformation sources and the surface geodetic measurements are captured by the Green's functions \mathbf{G}_{s} and \mathbf{G}_{e} , which are constructed based on analytical or semi-analytic solutions (Meade, 2007; Barbot, 2018). The \mathbf{R} matrix linking the translation and rotation with the observations can be formulated based on rotation on the spherical Earth's surface

$$\Omega = \begin{bmatrix} -r\cos\lambda\sin\varphi & -r\sin\lambda\sin\varphi & r\cos\varphi \\ r\sin\lambda & -r\cos\lambda & 0 \end{bmatrix}, \tag{2}$$

where r is the local radius of the earth, and φ and λ are the latitude and longitude of the GNSS station, respectively.

For the volume elements, we consider only three components of horizontal strain rate e_{nn} , e_{ee} , and e_{ne} expressed in the northeast coordinate system. The vertical measurements in Eastern China are sparse and involve large uncertainties. In addition, local vertical deformation of tectonic origin can be captured in the model by the motion of faults. Therefore, as a first-order approximation, we ignore the vertical strain components in the lower crust. As a result, the volume conservation of anelastic strain-rate simplifies to $e_{nn} + e_{ee} = 0$ and each volume element has two degrees of freedom. We allow displacement in the strike and dip directions for all fault patches. The meshing strategy results in a large number of model unknowns, related to 2 degrees of freedom on 2,551 volume elements, 2 slip components on 816 triangular surface elements, and 3 unknowns for spin rates. Given two velocity components at 955 GNSS positions, solving Equation (1) is an under-determined inverse problem. We employ Tikhonov regularizations (Aster et al., 2018) for slip and strain, with geological slip rates \mathbf{s}_* serving as additional constraints for slip-rate. The regularized inverse problem seeks to minimize the cost function

$$U = \|\mathbf{W}(\mathbf{d} - \mathbf{G}_{e}\mathbf{e} - \mathbf{G}_{s}\mathbf{s} - \mathbf{R}\boldsymbol{\omega})\|^{2} + \alpha^{2}\|\mathbf{e}\|^{2} + \beta^{2}\|\mathbf{L}\mathbf{s}\|^{2}, \quad \mathbf{s} \leq \mathbf{s}_{*}$$
(3)

In this equation, the first term quantifies the misfit between the model and the data, where $\bf W$ is a diagonal matrix with the inverse of measurement uncertainties, so that higher weights are given to the data with smaller uncertainties. The second and third terms respectively describe the roughness of the strain field and fault slip, with $\bf L$ being a finite difference approximation of the Laplacian operator, α and β being regularization parameters that balance the trade-off between data fitting and model roughness (see Fig. S2). The applied condition for slip rate ensures the compliance of the kinematic model with geological observations of long-term slip-rate. We utilize the least-squares method (Tarantola, 2005) to minimize the cost function in Equation (3), and we select the regularization parameters based on the L-curve criterion (Fig. S2). By minimizing the cost function with given α and β , we

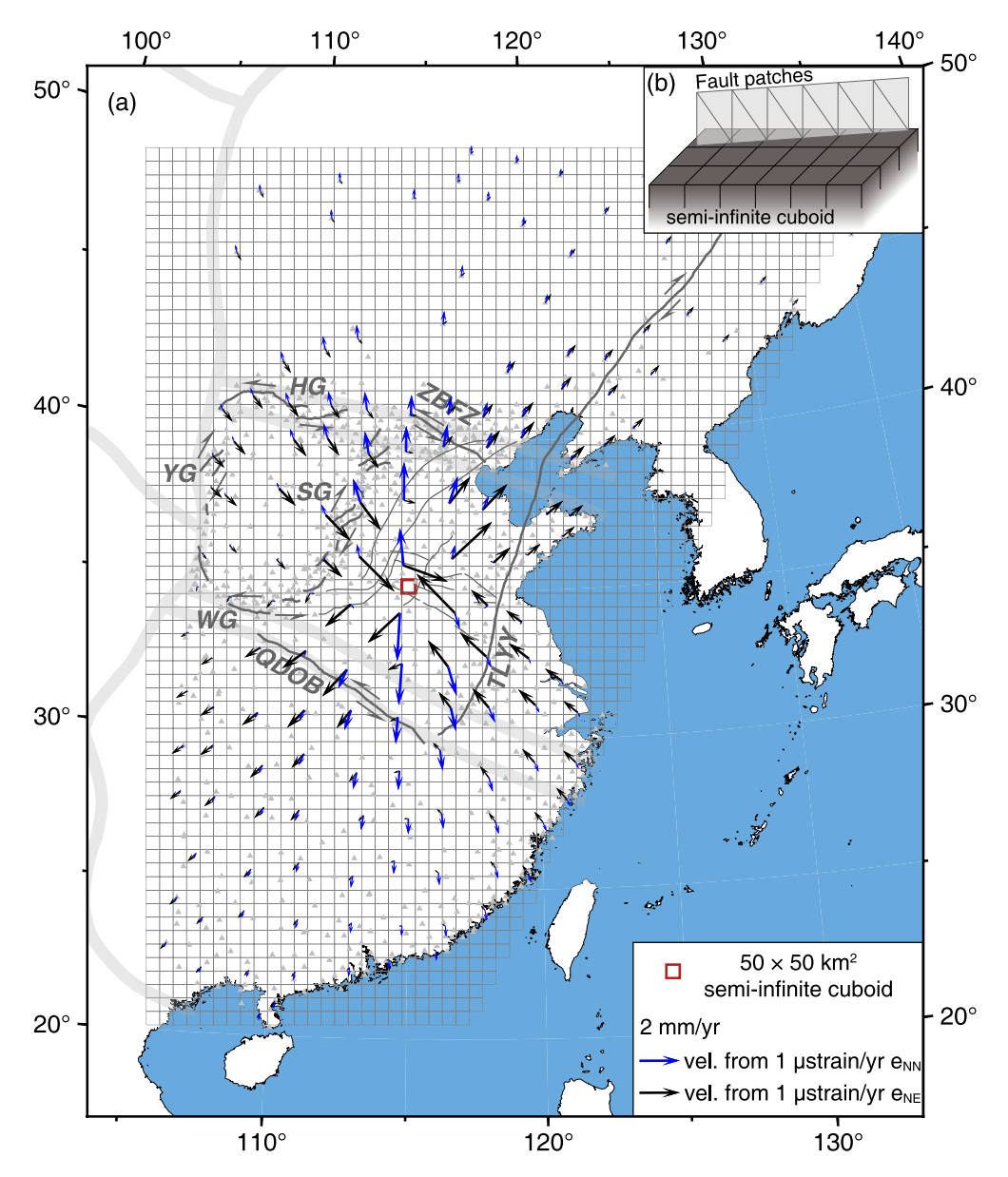


Fig. 2. Kinematic model setup and example Green's function. (a) Surface deformation associated with distributed plastic strain in a semi-infinite $50 \times 50 \text{ km}^2$ cuboid (red square) at 25 km depth. The blue and black vectors correspond to the surface velocities due to the horizontal strain-rate e_{nn} and e_{ne} in the red-marked element, respectively. Both e_{nn} and e_{ne} are 1 microstrain/yr. The underlying mesh of volume elements used to model distributed deformation is shown in the background. (b) Schematic diagram of the modeling setup. Deformation beneath the seismogenic upper crust localized along faults is represented as slip on triangular surface elements. Deformation in the lower crust and upper mantle related to distributed deep shear zones are discretized as strain-rate tensors in semi-infinite cuboidal elements.

obtain a model that balances the misfit and the roughness of the model parameters.

4. Geodetic data and model resolution

We use the most recent release of the geodetic velocity field of continental China (Wang and Shen, 2020), captured by the Crustal Movement Observation Network of China operating since the 1990s (e.g., Zhao et al., 2015; Zheng et al., 2017). In this dataset, the coseismic and postseismic displacements caused by $Mw \geq 5.9$ earthquakes have been corrected based on modeling of individual earthquakes (Wang and Shen, 2020). Thus, the velocity field represents the deformation of the stable interseismic phase related to tectonic motion. The selection based on a polygonal region for Eastern China results in 955 GNSS stations (Fig. 3).

We use checkerboard tests to investigate the resolution of the adopted GNSS network and the validity of the inversion method. Since the deformation in the plastic substrate is dominant and occurs presumably in the entire region, we consider the plastic strain rate as the deformation source. We test two checkerboards of different sizes (Fig. 4), using the synthetic strain rate e_{nn} of 15 nanostrain/yr on the elements marked with black dots and 0 otherwise (Fig. 4) to generate the synthetic surface velocities, via the product of Green's function \mathbf{G}_e and synthetic strain rate. Random noise, generated in the range of $\pm 10\%$ synthetic velocities, is taken as measurement uncertainties. We use the same regularization parameters used for modeling the real geodetic observations. The retrieved strain rate may explain $\sim 92\%$ of the synthetic velocities, in terms of variance reduction $(1-\sqrt{\sum \left(\mathbf{d}_{syn}-\mathbf{d}_{mod}\right)^2/\sum \mathbf{d}_{syn}^2}$, with \mathbf{d}_{syn} and \mathbf{d}_{mod} being the synthetic and modeled velocities, respectively), and provides the root mean square misfit χ_{rms} of ~ 1.2 ($\chi_{rms} = \sqrt{\frac{1}{n}\sum_{i=1}^n \left[\left(d_i^{syn}-d_i^{mod}\right)/s_i\right]^2}$, n is the number of velocity

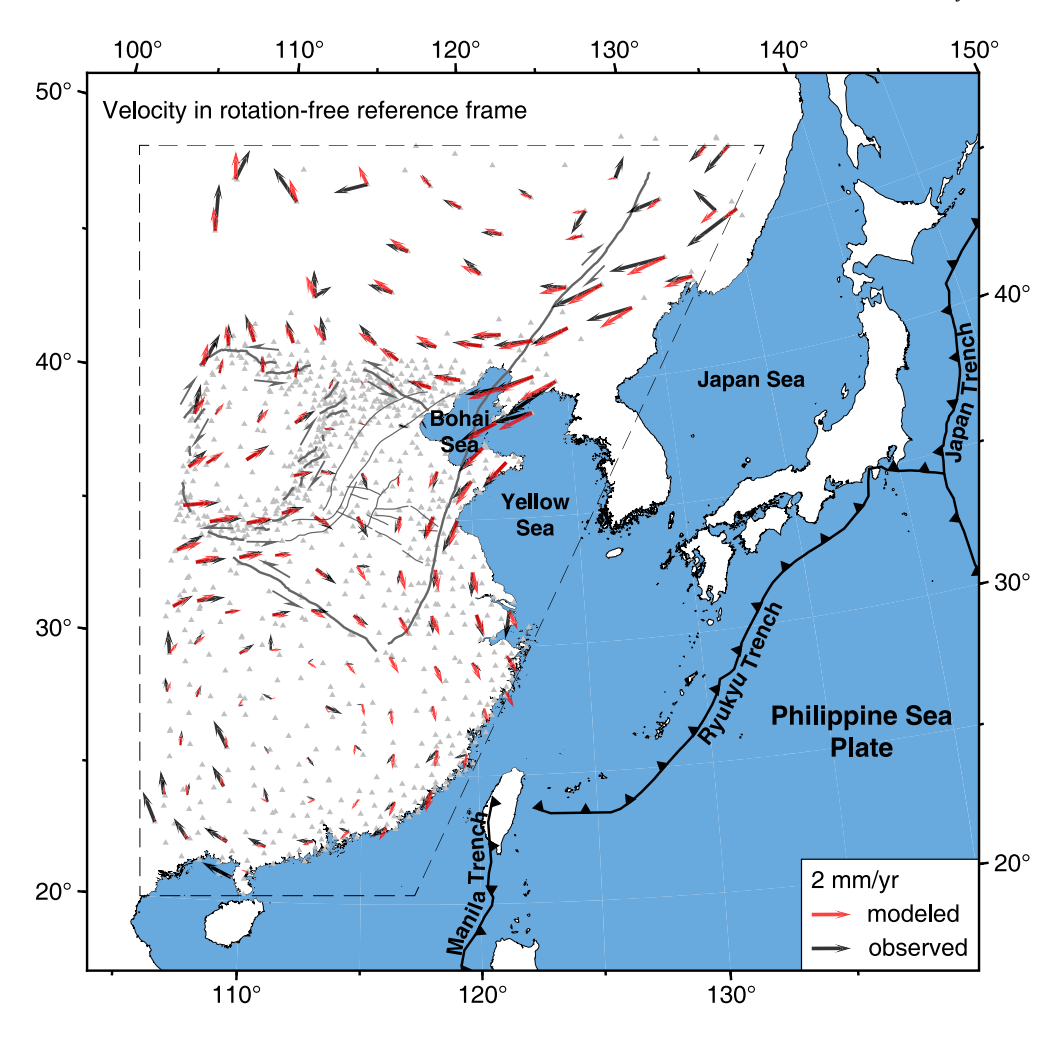


Fig. 3. The adopted GNSS network (gray triangle) and down-sampled velocity vectors in a rotation-free reference frame, i.e., after eliminating the translation and rotation described by ω in Equation (1). The velocity field is down-sampled in this figure only for illustration purposes. The large discrepancies in the AB are mainly due to larger data uncertainty (Fig. S3).

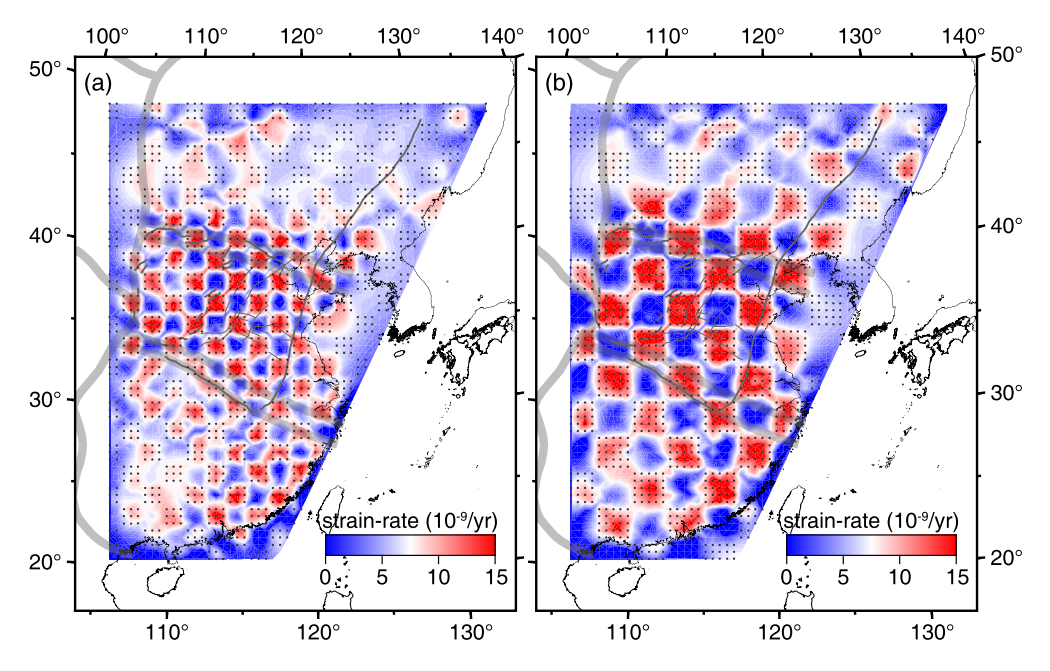


Fig. 4. Checkerboard tests with the adopted GNSS network. (a) 3×3 checkerboard test, testing a spatial resolution of resolution of 150 km. (b) 5×5 checkerboard test, testing a spatial resolution of 250 km. We apply 15 nanostrain/yr on the elements marked with black dots and 0 otherwise.

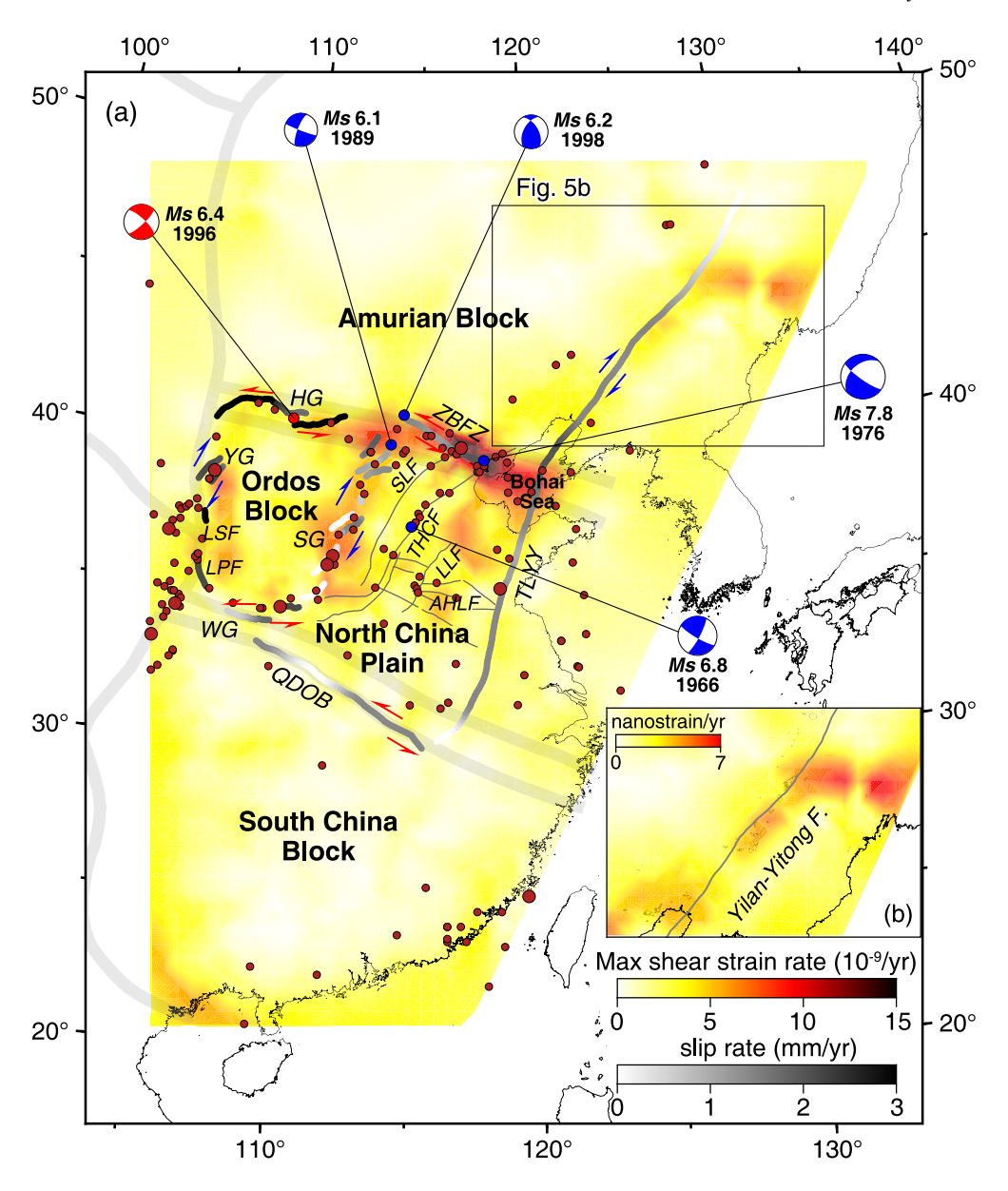


Fig. 5. Kinematic model of Eastern China. (a) The maximum shear strain-rate in the plastic substrate and the along-strike average of fault slip rate in the upper and middle crust are color-coded accordingly. The red dots are the $M \ge 6$ crustal earthquakes, identical to Fig. 1. (b) The strain rate surrounding the Yilan-Yitong fault is displayed as a highlight.

data and s_i is the uncertainty of the *i*th velocity datum), implying that the inversion is robust.

The results provide inhomogeneous spatial resolutions related to the density of surface observations. The GNSS network affords a resolution of $\sim\!150$ km to the NCB and the SCB, but a coarser resolution of $\sim\!250$ km to the AB with a relatively better resolution around the Yilan-Yitong fault, as suggested by the comparison between two checkerboard tests using different sizes. Although these observations are unsuited to resolve detailed along-fault kinematics, they are suitable for capturing large-scale tectonic features.

5. Crustal deformation of Eastern China

The kinematic model (Fig. 5), consisting of distributions of fault slip rate and strain rate of plastic substrate, explains the surface velocity field well (Fig. 3), with an overall variance reduction of \sim 87%, a χ_{rms} of \sim 1.48, and a mean residual velocity of \sim 0.64 mm/yr. The residuals exhibit little spatial coherence (Fig. S3). We demonstrate the slip rate averaged over depth in Fig. 5, delineating

first-order fault kinematics. Detailed spatial distributions of fault slip and the underlying two components of the strain tensors can be found in Figs. S4 and S5. Apart from the translation and rotation, which account for \sim 78% of the observed velocity field in terms of variance reduction, the remaining internal deformation is partitioned by on-fault slip (\sim 1%) and distributed strain (\sim 9%). Ignoring the rigid-body component of the velocity field, the deformation is caused by fault slip (10%) and distributed strain (90%). Given the importance of the latter component, we focus the interpretation on the deep-seated deformation.

The plastic deformation of Eastern China concentrates primarily in and around the NCB, with the largest shear strain rate of ~ 15 nanostrain/yr, at the similar level as that derived directly from velocity gradient (Wang and Shen, 2020). In contrast, the shear strain-rate in the AB and the SCB is only a few nanostrain/yr or less. Continental-scale strain localization along part of the HG, the seismically active ZBFZ, and the Bohai Sea forms a continuous, transcontinental NW-striking shear zone that decouples the AB from the NCB. Strain along the SG forms an NNE-striking shear

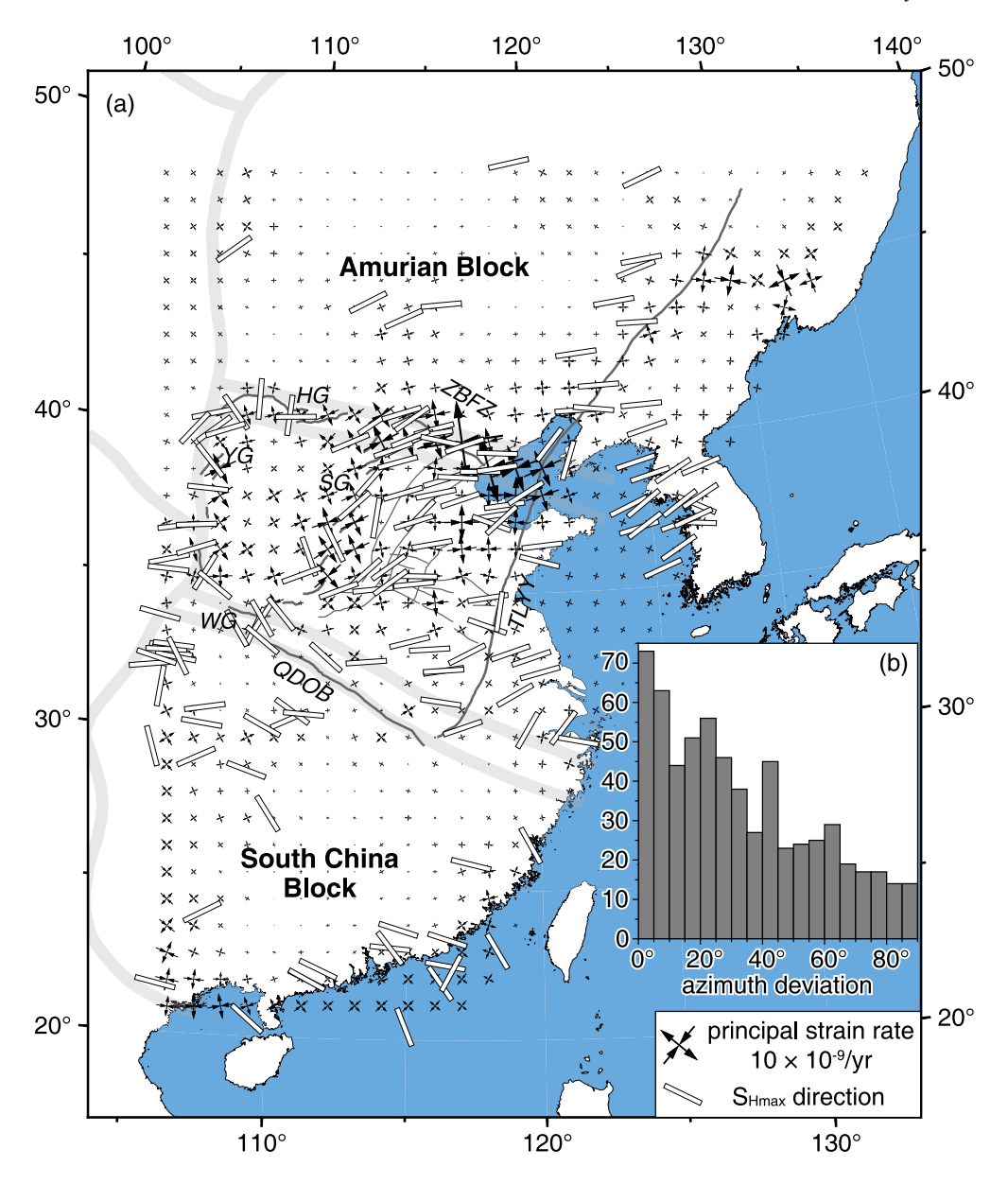


Fig. 6. Orientations of the modeled principal strain rate and the principal compressive stress from the WSM project (Heidbach et al., 2018). (a) Modeled principal strain rates (down-sampled) are represented by vector pairs, and open bars indicate the orientation of principal horizontal compressive stress (S_{Hmax}). (b) Orientation differences between the S_{Hmax} and the modeled principal compression.

zone at the margin of the NCP and OB. The western and southwestern margins of the OB are identified with strain localization nearly collocated with the YG, the LSF and the LPF. As the shear zones stretch hundreds of kilometers, well above the resolution level of the adopted GNSS network (Fig. 4), they can be considered robust tectonic features. A major shear zone cannot be found along the QDOB and WG, despite their structural importance as the suture between the NCB and SCB. A shear zone could have formed below the Yilan-Yitong fault (Fig. 5b), but with a much lower amplitude than those mentioned above. Within the NCP, strain localization may be present in separate regions, but not well shaped into long, continuous strain belts.

To test the compatibility of the modeled distributed deformation with the stress state in the brittle crust, we compare the direction of the inferred plastic strain-rate with the direction of maximum horizontal compressive stress (S_{Hmax}) of the World Stress Map (WSM) database (Fig. 6, Heidbach et al. (2018)). We select the principal compressive strain-rate of the volume element nearest to the stress measurement point and calculate the azimuth deviation

between the S_{Hmax} and the principal compressive strain-rate, the majority of S_{Hmax} measurements align with the principal compressive strain within $\pm 30^\circ$ (Fig. 6b), which suggests a broad coherence of crustal deformation of different source with the modeled plastic strain field. Larger deviations happen in the AB and SCB with negligible deformation, subject to potentially larger uncertainties involved in the orientations of both WSM stress and our modeled strain field.

6. Discussion

 $6.1. \ Sinistral$ and dextral shear zones resolved from the plastic strain field

Earthquakes occur as a consequence of rapid release of frictional stress imposed by secular shear in response to deep and far-field tectonic loading. To better characterize the orientation of shear in the plastic substrate, we decompose the strain-rate tensor into two conjugate directions of maximum shear compatible with

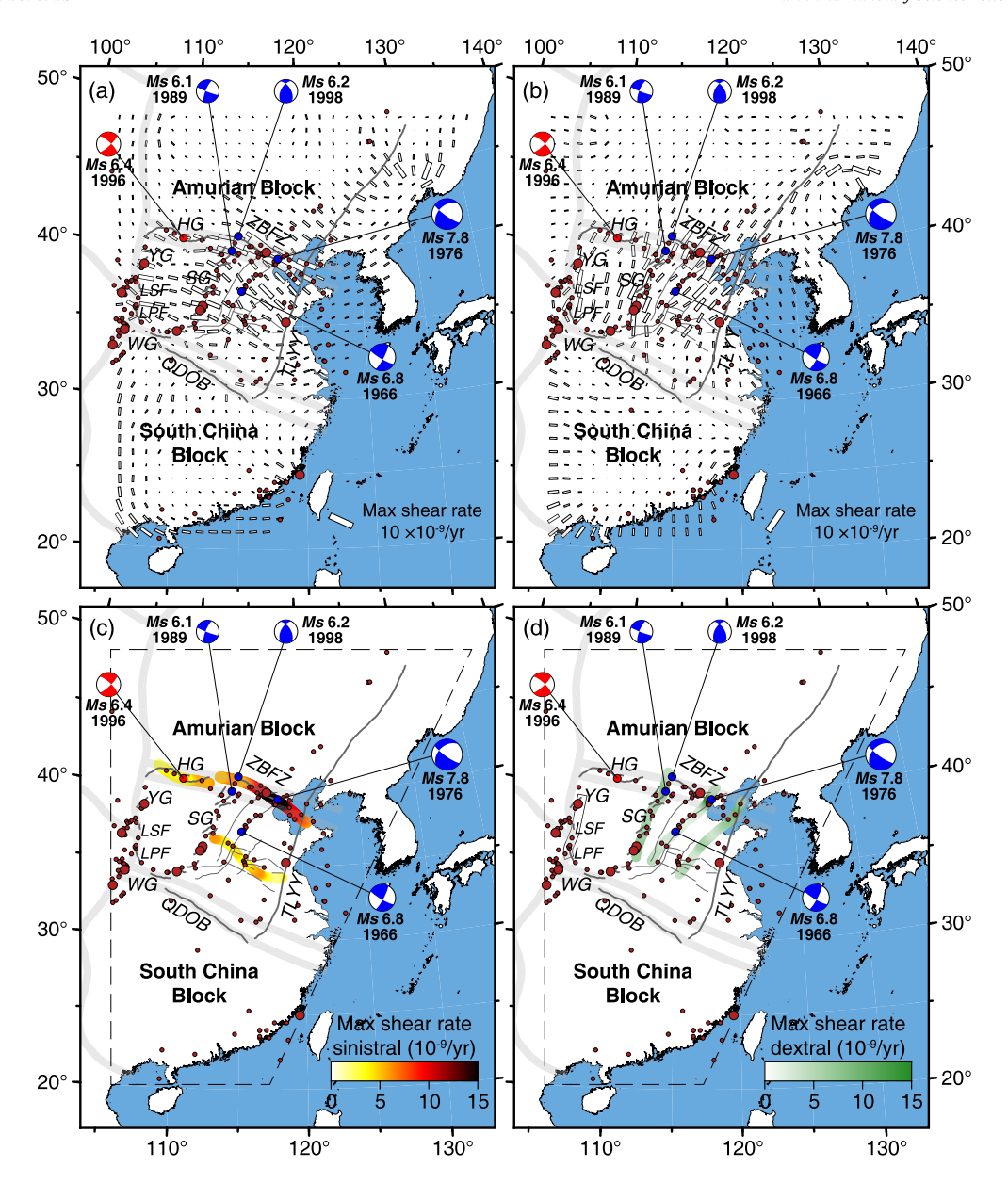


Fig. 7. Distribution of maximum shear of the modeled plastic strain-rate tensor. (a) Maximum sinistral shear. The open bars represent the magnitude and direction of down-sampled shear strain-rates. (b) Maximum dextral shear. (c) Left-lateral shear zones constructed based on streamlines of shear strain-rate in panel (a). (d) Similar to (c), but for right-lateral shear zones. The open belt along the western border of the OB represents a simple shear belt formed based on the strain alignment is ambiguous because of the complex geological structures here.

left-lateral (Fig. 7a) and right-lateral (Fig. 7b) faulting. Some shear zones stand out in and around the NCB, particularly the left-lateral shear margining the AB and NCB, and right-lateral shear margining the OB and NCP, all of which collocated with the surficial fault structures.

Describing the velocity gradient using volume elements in pure shear allows us to capture the spatial variations of deformation. However, the horizontal alignment of individual elements deforming in pure shear with similar principal directions may form a coherent tectonic structure deforming in simple shear. To identify such possible shear zones, we build streamlines of the maximum shear strain-rates. We consider thresholds of 1 nanostrain/yr and the length of 400 km to capture the regional-scale structures. Details on constructing streamlines of maximum shear strain-rates can be found in the supplementary materials.

The constructed streamlines depict two significant EW-trending left-lateral shear zones encompassing the seismic belts of ZBFZ and HG (Fig. 7c) that accommodate the relative motion between the

AB and the NCB. Another EW-trending left-lateral shear zone in Fig. 7c stretches across the central NCP, coinciding with the seismic belts of AHLF. A series of NNE-trending right-lateral shear zones are found conjugate to the left-lateral shear zones (Fig. 7d), forming a bookshelf structure that coincides with the seismically active faults (Zhang et al., 2018), e.g., the SG and the THCF that generated the 1966 Ms 6.8, 1976 Ms 7.8, and 1989 Ms 6.1 earthquakes. The strain alignment along the Yilan-Yitong fault suggests the formation of a right-lateral shear zone underneath (Figs. 7b and S6). The formation of a simple shear zone based on the alignment of strains at the western margin of the OB is ambiguous (Fig. 7d), because the tectonics there involves both dextral (e.g., the YG and the LSF) and sinistral (e.g., the LPF) faulting.

These shear zones constitute major regional-scale structures that accommodate regional kinematics and drive seismicity in the brittle crust. The HG left-lateral shear zone extends \sim 400 km and the ZBFZ left-lateral shear zone extends \sim 740 km. The AHLF left-lateral shear zone stretches \sim 600 km from the SG to TLYY. The

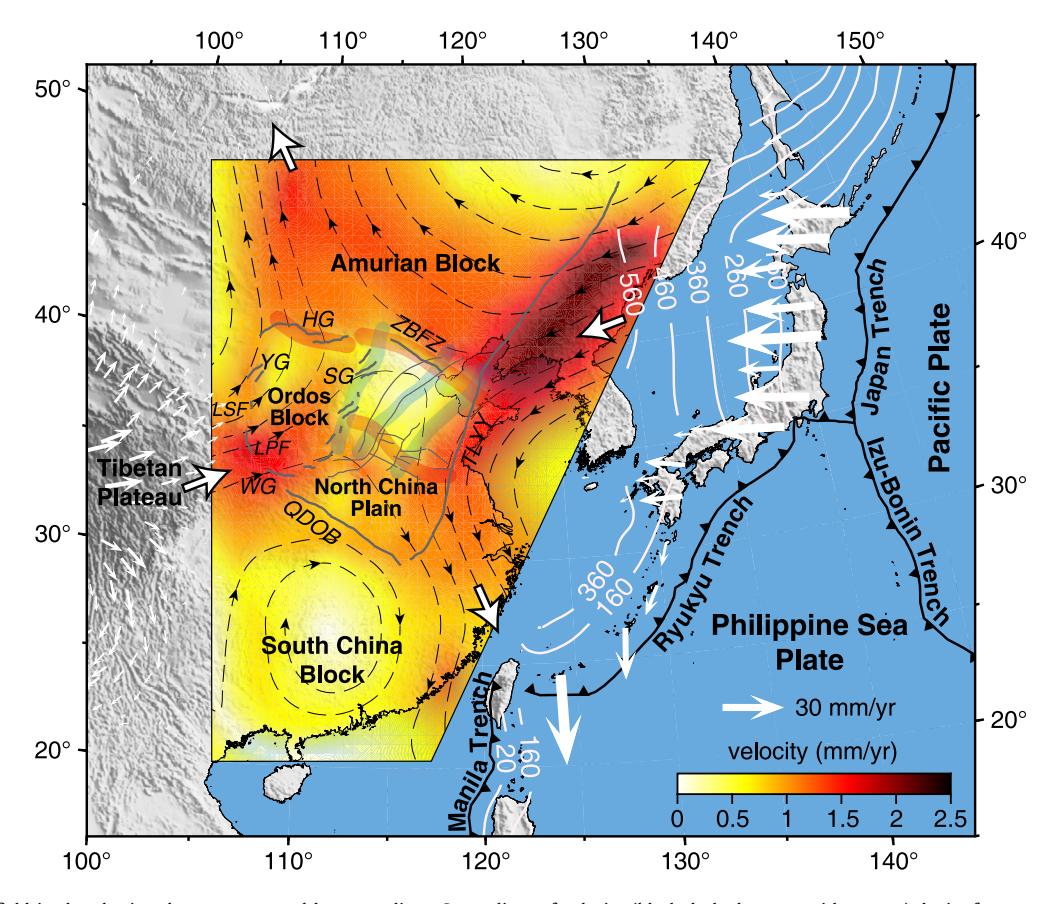


Fig. 8. The velocity field in the plastic substrate expressed by streamlines. Streamlines of velocity (black dashed curves with arrows) depict four separate trajectories partitioned by the axes of principal compression and extension (white arrows with black outlines) in the Eastern China fixed reference frame (rotation-free reference, same as Fig. 3). The color belts are the shear zones constructed from strain field (Fig. 7). The white contours indicate the subducting slab of the Pacific plate and the Philippine Sea plate (Hayes et al., 2018). The peripheral GNSS velocities in the same reference frame as the streamlines are displayed in white. These velocities determined from the displacement measurements between 1996 and 2015 (Hao et al., 2019) have been corrected for the deformation related to earthquakes and may represent deep-seated tectonic motion.

NNE-striking right-lateral shear zones slice the NCP roughly in parallel, extending \sim 700 km from the AHLF to ZBFZ. Remarkably, the shear zones overlap with the major strike-slip faults and encompass virtually all the historical and instrumental $M \geq 6$ earth-quakes in and around the NCB, explaining the recent seismic activity in Eastern China. The strain-rate near the epicenter of the 1976 Ms 7.8 Tangshan earthquake is still elevated, consistent with the frequent occurrence of moderate earthquakes in recent years.

At block boundaries, such as the HG and ZBFZ margining the AB and NCB, and the SG margining the OB and NCP, the shear zones are characterized by a long alignment of similarly oriented high-amplitude strain-rate. In contrast, the secondary shear zones, such as the THCF and AHLF inside the NCP, exhibit only moderate strain-rate, despite being continuously aligned. Previous analyses based solely on the strain amplitude may have overlooked the secondary shear zones and their potential to generate large earth-quakes, which is also supported by studies of active tectonics (Yin et al., 2014).

6.2. North China as a mechanical bridge linking Pacific subduction and extrusion of the Tibetan Plateau

To unveil the contemporaneous tectonic deformation of Eastern China and its link with the surrounding kinematics, we produce a continuous velocity field in the plastic substrate by integrating the plastic strain-rate (Fig. 8). The streamlines of the velocity field give away regional-scale shear in two conjugate directions centered on the NCP. The regional deformation is accommodated by two pairs of shear zones, respectively related to the sinistral ZBFZ and AHLF

in the north and south, a dextral shear zone parallel to the THCF in the east and the SG in the west. The shear zones cause an abrupt velocity changes across the NCB. In addition, the velocity changes in both amplitude and directions across the northern margin of the OB due to sinistral shear along the HG.

The QDOB and WG delineate the margin between the NCB and SCB. Yet, they do not behave as important shear zones like ZBFZ, and demonstrate both slow slip rate and slow strain rate, contrary to expectations for such an important block boundary (Fig. 5). Instead, they locate in a wide zone of high velocity with little internal deformation. Seismic tomography indicates thinner crust below the QDOB and WG (Bao et al., 2013), as well as low seismic velocity anomalies in the lower crust and upper mantle (Guo and Chen, 2016; Li et al., 2017; Wei et al., 2022), likely attributed to material extrusion below the high Tibetan plateau. The margin between the NCB and the SCB may be more diffuse than previously thought, with sinistral shear occurring further north, below the AHLF.

The principal axes of the regional finite strain-rate (white arrows with black outlines in Fig. 8) may conveniently partition the velocity field into four separate trajectories. The principal compression coincides with the northeastward extrusion of the Tibetan Plateau at the latitude of the OB and the westward subduction of the Pacific plate at the latitude of the AB, while the principal extension direction aligns with the retreat of the Philippine Sea plate below the Ryukyu trench, as illuminated by the peripheral GNSS vectors (white-bold arrows in Fig. 8, (Hao et al., 2019)) relative to fixed Eastern China, i.e., in the same reference frame as the streamlines.

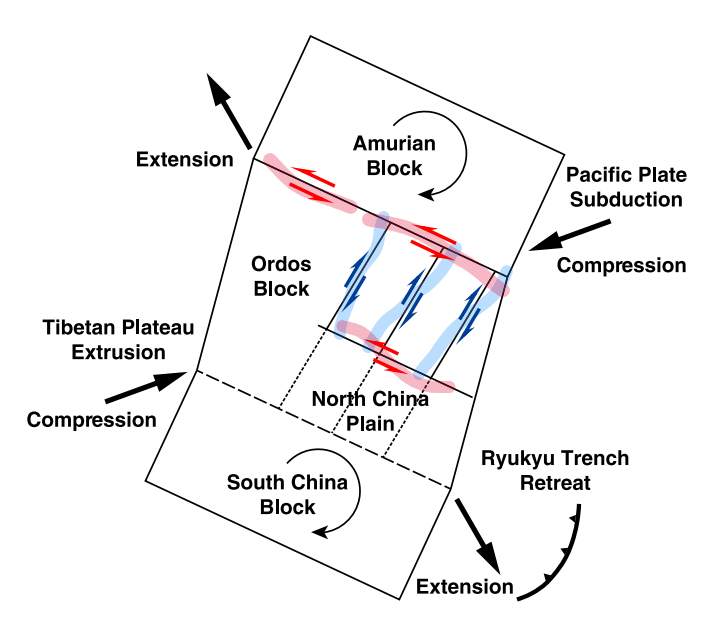


Fig. 9. Simplified structural model of Eastern China in the context of regional tectonics. The NCB acts as a mechanical bridge linking the mobile Tibetan plateau, the Pacific plate, and the Philippine Sea plate below the Ryukyu trench, and accommodates their relative motion by conjugate shear zones in and around the NCB, and particularly the NCP.

The North China Block, as a mechanical bridge between distant boundary conditions, links the kinematics of the neighboring plates in all cardinal directions (Figs. 8 and 9). To the north, the Pacific plate subducts westwards, in alignment with the streamlines, as captured by the stable GPS velocities in Japan Arc derived from the two-decade displacement measurements between 1996 and 2015 (Hao et al., 2019) converted into the same reference frame as the streamlines. The subduction at this latitude is relatively gentle, with the western edge of stagnant slab reaching the location of the Yilan-Yitong fault (Huang and Zhao, 2006; Hayes et al., 2018). The higher velocity concentrated east of the Yilan-Yitong fault supports its significance as a tectonic margin (Min et al., 2013; Xu et al., 2017). The corresponding driving force may originate from the subduction of the Pacific plate, resulting in right-lateral shear across the Yilan-Yitong fault. The homogeneous velocity field west of the Yilan-Yitong fault and north of the ZBFZ and HG reflects the left-lateral motion of the virtually rigid AB relative to the NCB, also driven by the subducting Pacific plate. To the west, material extrusion from the northeastern Tibetan plateau aligning with the left-lateral faults (e.g., the Haiyuan fault and QDOB) occurs in the southwest of the OB. At the latitude of the OB, the Tibetan plateau extrudes opposite to the Pacific plate subduction, forming a northeast-southwest large-scale compression throughout the NCB. The compressional moment, in conjunction with the retreat of the Philippine Sea plate below the Ryukyu trench, creates farfield boundary conditions leading to the passive deformation of the NCB. The deformation of Eastern China is accommodated by conjugate shear zones in and around the NCB, particularly inside the NCP, compatible with previous findings (e.g., Briais et al., 1993; Peltzer and Saucier, 1996).

The internal deformation of the NCB fills the space problem posed by the subducting Pacific plate underneath the AB with simultaneous retreat of the Philippine Sea plate below the Ryukyu trench and the tectonic escape of the Tibetan plateau (Fig. 9). The sinistral shear zones of the NCB accommodate the left-lateral motion of the Pacific plate relative to the tectonic escape of the Tibetan plateau and the retreating Philippine Sea plate, while the dextral shear zones modulate the regional stress and take up the differential motion between the Pacific plate and the Philippine

Sea plate below the Ryukyu trench, resulting in the occurrence of frequent destructive earthquakes along the fault zones within and around the NCB.

7. Conclusions

We construct a kinematic model to understand the tectonic setting underlying the destructive earthquakes of North China. The suture between the NCB and SCB may not be currently deforming, with left-lateral shear on parallel E-W structures occurring farther north. Instead, strain concentrates in and around the NCB, forming east-west oriented left-lateral shear zones along the HG and the ZBFZ that decouple the AB from the NCB. A secondary left-lateral shear zone transecting the NCP is collocated with the AHLF. Its combination with a series of NNE-NE oriented right-lateral shear zones creates bookshelf deformation in the NCP. These shear zones coincide with large historical earthquakes. The North China Block, circumscribed by the westward subduction of the Pacific plate at the latitude of the AB, the northeastward extrusion below the Tibetan plateau at the latitude of the OB and the retreat of the Philippine Sea plate below the Ryukyu trench, acts as a mechanical bridge that modulates the relative motion of the surrounding mobile tectonic units, leading to frequent destructive earthquakes.

CRediT authorship contribution statement

Fengming Shen: Writing – original draft, Visualization, Formal analysis. **Lifeng Wang:** Writing – review & editing, Supervision, Methodology, Conceptualization. **Sylvain Barbot:** Writing – review & editing, Software, Methodology. **Jiahong Xu:** Investigation, Data curation.

Declaration of competing interest

The authors declare that they have no known competing financial interests or personal relationships that could have appeared to influence the work reported in this paper.

Data availability

The GNSS velocities used for this study and the modeled strainrate are provided in supplementary materials.

Acknowledgements

We thank Wang and Shen (2020) for making the velocity data available and the anonymous reviewers for their constructive comments. This work is supported by Grants from the National Natural Science Foundation of China [U2239204, U1839211] and the Central Public-interest Scientific Institution Basal Research Fund [IGCEA2006]. SB is supported in part by the National Science Foundation under award number EAR-1848192. All figures are drawn using GMT (Wessel et al., 2019).

Appendix A. Supplementary material

Supplementary material related to this article can be found online at https://doi.org/10.1016/j.epsl.2023.118407.

References

Aster, R.C., Borchers, B., Thurber, C.H., 2018. Parameter Estimation and Inverse Problems, 3rd ed. Elsevier, Amsterdam.

Avouac, J.-P., 2015. From geodetic imaging of seismic and aseismic fault slip to dynamic modeling of the seismic cycle. Annu. Rev. Earth Planet. Sci. 43 (1), 233–271. https://doi.org/10.1146/annurev-earth-060614-105302.

- Bao, X., Song, X., Xu, M., Wang, L., Sun, X., Mi, N., et al., 2013. Crust and upper mantle structure of the North China Craton and the NE Tibetan Plateau and its tectonic implications. Earth Planet. Sci. Lett. 369–370, 129–137. https://doi.org/ 10.1016/j.epsl.2013.03.015.
- Barbot, S., 2018. Deformation of a half-space from anelastic strain confined in a tetrahedral volume. Bull. Seismol. Soc. Am. 108 (5A), 2687–2712. https://doi.org/10.1785/0120180058.
- Barbot, S., 2020. Mantle flow distribution beneath the California margin. Nat. Commun. 11 (1), 4456. https://doi.org/10.1038/s41467-020-18260-8.
- Barbot, S., Weiss, J.R., 2021. Connecting subduction, extension and shear localization across the Aegean Sea and Anatolia. Geophys. J. Int. 226 (1), 422–445. https:// doi.org/10.1093/gji/ggab078.
- Bolt, B.A., 1985. Catalog of Chinese Earthquakes (1831 BC-1969 AD): Gu Gong-xu, Lin Ting-huang, Zhu Chen-liung, and others, Academia Sinica, Scientific Publishing House, Peking, 1983, 894 pp. Bulletin of the Seismological Society of America 75 (1), 335. https://doi.org/10.1785/BSSA0750010335.
- Briais, A., Patriat, P., Tapponnier, P., 1993. Updated interpretation of magnetic anomalies and seafloor spreading stages in the South China Sea: implications for the Tertiary tectonics of southeast Asia. J. Geophys. Res., Solid Earth 98 (B4), 6299–6328. https://doi.org/10.1029/92|B02280.
- Chen, W.P., Nabelek, J., 1988. Seismogenic strike-slip faulting and the development of the North China Basin. Tectonics 7 (5), 975–989. https://doi.org/10.1029/TC007i005p00975.
- Deng, Q., Cheng, S., Min, W., Yang, G., Reng, D., 1999. Discussion on Cenozoic tectonics and dynamics of ordos block. J. Geomech. 5 (3), 13–21. (in Chinese with an English abstract).
- Dong, Y., Ni, S., Yuen, D.A., Li, Z., 2018. Crustal rheology from focal depths in the North China Basin. Earth Planet. Sci. Lett. 497, 123–138. https://doi.org/10.1016/ i.epsl.2018.06.018.
- Elliott, J.R., Walters, R.J., Wright, T.J., 2016. The role of space-based observation in understanding and responding to active tectonics and earthquakes. Nat. Commun. 7, 13844. https://doi.org/10.1038/ncomms13844.
- Garfunkel, Z., 1974. Model for the late Cenozoic tectonic history of the Mojave Desert, California, and for its relation to adjacent regions. Geol. Soc. Am. Bull. 85 (12), 1931–1944. https://doi.org/10.1130/0016-7606(1974)85<1931:MFTLCT>2.0.
- Guo, H., Zhao, J., 2019. The surface rupture zone and paleoseismic evidence on the seismogenic fault of the 1976 Ms 7.8 Tangshan earthquake, China. Geomorphology 327, 297–306. https://doi.org/10.1016/j.geomorph.2018.11.006.
- Guo, Z., Chen, Y.J., 2016. Crustal structure of the eastern Qinling orogenic belt and implication for reactivation since the Cretaceous. Tectonophysics 683, 1–11. https://doi.org/10.1016/j.tecto.2016.06.007.
- Han, Z., Xu, J., Ran, Y., Chen, L., Yang, X., 2003. Active blocks and strong seismic activity in North China region. Sci. China, Ser. D, Earth Sci. 46 (2), 153–167. https://doi.org/10.1360/03dz0012.
- Hao, M., Li, Y., Zhuang, W., 2019. Crustal movement and strain distribution in East Asia revealed by GPS observations. Sci. Rep. 9 (1), 16797. https://doi.org/10. 1038/s41598-019-53306-y.
- Hayes, G.P., Moore, G.L., Portner, D.E., Hearne, M., Flamme, H., Furtney, M., Smoczyk, G.M., 2018. Slab2, a comprehensive subduction zone geometry model. Science 362 (6410), 58–61. https://doi.org/10.1126/science.aat4723.
- He, J., Liu, M., Li, Y., 2003. Is the Shanxi rift of northern China extending? Geophys. Res. Lett. 30 (23). https://doi.org/10.1029/2003gl018764.
- Heidbach, O., Rajabi, M., Cui, X., Fuchs, K., Müller, B., Reinecker, J., et al., 2018. The world stress map database release 2016: crustal stress pattern across scales. Tectonophysics 744, 484–498. https://doi.org/10.1016/j.tecto.2018.07.007.
- Holt, A.F., Royden, L.H., Becker, T.W., Faccenna, C., 2018. Slab interactions in 3-D subduction settings: the Philippine Sea plate region. Earth Planet. Sci. Lett. 489, 72–83. https://doi.org/10.1016/j.epsl.2018.02.024.
- Huang, J., Zhao, D., 2006. High-resolution mantle tomography of China and surrounding regions. J. Geophys. Res. 111 (B9). https://doi.org/10.1029/ 2005jb004066.
- Laske, G., Masters, G., Ma, Z., Pasyanos, M., 2013. Update on CRUST1. 0—a 1-degree global model of Earth's crust. Paper presented at the Geophys. Res. Abstr.
- Li, Y., Wang, X., Zhang, R., Wu, Q., Ding, Z., 2017. Crustal structure across the NE Tibetan Plateau and Ordos Block from the joint inversion of receiver functions and Rayleigh-wave dispersions. Tectonophysics 705, 33–41. https://doi.org/10.1016/j. tecto.2017.03.020.
- Liu, D., Nutman, A., Compston, W., Wu, J., Shen, Q.H., 1992. Remnants of ≥ 3800 Ma crust in the Chinese part of the Sino-Korean craton. Geology 20 (4), 339–342. https://doi.org/10.1130/0091-7613(1992)020<0339:ROMCIT>2.3.CO;2.
- Liu, Y., Liu, L., Li, Y., Peng, D., Wu, Z., Cao, Z., et al., 2022. Global back-arc extension due to trench-parallel mid-ocean ridge subduction. Earth Planet. Sci. Lett. 600. https://doi.org/10.1016/j.epsl.2022.117889.
- Luo, Y., Xu, Y., Yang, Y., 2012. Crustal structure beneath the Dabie orogenic belt from ambient noise tomography. Earth Planet. Sci. Lett. 313–314, 12–22. https:// doi.org/10.1016/j.epsl.2011.11.004.
- Meade, B.J., 2007. Algorithms for the calculation of exact displacements, strains, and stresses for triangular dislocation elements in a uniform elastic half space. Comput. Geosci. 33 (8), 1064–1075. https://doi.org/10.1016/j.cageo.2006.12.003.

- Meade, B.J., Loveless, J.P., 2009. Block modeling with connected fault-network geometries and a linear elastic coupling estimator in spherical coordinates. Bull. Seismol. Soc. Am. 99 (6), 3124–3139. https://doi.org/10.1785/0120090088.
- Meng, Q.-R., Wang, E., Hu, J.-M., 2005. Mesozoic sedimentary evolution of the northwest Sichuan basin: implication for continued clockwise rotation of the south China block. Geol. Soc. Am. Bull. 117 (3). https://doi.org/10.1130/b25407.1.
- Meng, Q.-R., Zhang, G.-W., 1999. Timing of collision of the North and south China blocks: controversy and reconciliation. Geology 27 (2), 123–126. https://doi.org/ 10.1130/0091-7613(1999)027<0123:TOCOTN>2.3.CO:2.
- Menzies, M., Xu, Y., Zhang, H., Fan, W., 2007. Integration of geology, geophysics and geochemistry: a key to understanding the North China Craton. Lithos 96 (1–2), 1–21. https://doi.org/10.1016/j.lithos.2006.09.008.
- Min, W., Liu, Y., Jiao, D., Shen, J., Pan, X., 2013. Evidence for Holocene activity of the Yilan-Yitong fault, northeastern section of the Tan-Lu fault zone in northeast China. J. Asian Earth Sci. 67–68, 207–216. https://doi.org/10.1016/j.jseaes.2013.02.031
- Pan, Y., Hammond, W.C., Ding, H., Mallick, R., Jiang, W., Xu, X., et al., 2021. GPS imaging of vertical bedrock displacements: quantification of two-dimensional vertical crustal deformation in China. J. Geophys. Res., Solid Earth 126 (4). https://doi.org/10.1029/2020jb020951.
- Peltzer, G., Saucier, F., 1996. Present-day kinematics of Asia derived from geologic fault rates. J. Geophys. Res., Solid Earth 101 (B12), 27943–27956. https://doi. org/10.1029/96/B02698.
- Royden, L.H., Burchfiel, B.C., van der Hilst, R.D., 2008. The geological evolution of the Tibetan Plateau. Science 321 (5892), 1054–1058. https://doi.org/10.1126/science. 1155371
- Shen, Z., Zhao, C., Yin, A., Li, Y., Jackson, D.D., Fang, P., Dong, D., 2000. Contemporary crustal deformation in East Asia constrained by global positioning system measurements. J. Geophys. Res., Solid Earth 105 (B3), 5721–5734. https://doi.org/10.1029/1999jb900391.
- Tan, X., Kodama, K.P., Gilder, S., Courtillot, V., Cogné, J.-P., 2007. Palaeomagnetic evidence and tectonic origin of clockwise rotations in the Yangtze fold belt, south China Block. Geophys. J. Int. 168 (1), 48–58. https://doi.org/10.1111/j.1365-246X. 2006.03195.x.
- Tarantola, A., 2005. Inverse Problem Theory and Methods for Model Parameter Estimation. Society for Industrial and Applied Mathematics, Philadelphia.
- Teng, J., Deng, Y., Badal, J., Zhang, Y., 2014. Moho depth, seismicity and seismogenic structure in China mainland. Tectonophysics 627, 108–121. https://doi.org/10.1016/j.tecto.2013.11.008.
- Thatcher, W., 2009. How the continents deform: the evidence from tectonic geodesy. Annu. Rev. Earth Planet. Sci. 37 (1), 237–262. https://doi.org/10.1146/annurev.earth.031208.100035.
- The Research Group on Active Fault System around Ordos Massif, State Seismological Bureau, 1988. Active fault system around Ordos Massif (in Chinese with an English contents). Seismological Press, Beijing.
- Wang, C., Wu, Q., Duan, Y., Wang, Z., Lou, H., 2017. Crustal and upper mantle structure and deep tectonic genesis of large earthquakes in North China. Sci. China Earth Sci. 60 (5), 821–857. https://doi.org/10.1007/s11430-016-9009-1.
- Wang, L., Barbot, S., 2023. Three-dimensional kinematics of the India–Eurasia collision. Commun. Earth Environ. 4 (1). https://doi.org/10.1038/s43247-023-00815-4.
- Wang, M., Shen, Z., 2020. Present-day crustal deformation of continental China derived from GPS and its tectonic implications. J. Geophys. Res., Solid Earth 125 (2). https://doi.org/10.1029/2019jb018774.
- Wei, Y., Zhang, S., Li, M., Wu, T., Hua, Y., Zhang, Y., Cai, J., 2022. Regional lithospheric deformation beneath the East Qinling-Dabie orogenic belt based on ambient noise tomography. Geophys. J. Int. 228 (2), 1294–1312. https://doi.org/10.1093/gji/ggab393.
- Wessel, P., Luis, J.F., Uieda, L., Scharroo, R., Wobbe, F., Smith, W.H.F., Tian, D., 2019. The generic mapping tools version 6. Geochem. Geophys. Geosyst. 20 (11), 5556–5564. https://doi.org/10.1029/2019gc008515.
- Wu, F.-Y., Yang, J.-H., Xu, Y.-G., Wilde, S.A., Walker, R.J., 2019. Destruction of the North China Craton in the Mesozoic. Annu. Rev. Earth Planet. Sci. 47 (1), 173–195. https://doi.org/10.1146/annurev-earth-053018-060342.
- Wu, Z., Zhou, C., Huang, X., Zhao, G., Tan, C., 2020. Main active faults and seismic activity along the Yangtze River economic belt: based on remote sensing geological survey. China Geol. 3 (2), 314–338. https://doi.org/10.31035/cg2020041.
- Xiao, W., Windley, B.F., Han, C., Liu, W., Wan, B., Zhang, J.e., et al., 2018. Late Pale-ozoic to early Triassic multiple roll-back and oroclinal bending of the Mongolia collage in central Asia. Earth-Sci. Rev. 186, 94–128. https://doi.org/10.1016/j.earscirev.2017.09.020.
- Xu, J., Ji, F., 2015. Structure of the Bohai Bay basin and its evolution (in Chinese with an English contents). Seismological Press, Beijing.
- Xu, J., Song, C., Chu, Q., 1998. Preliminary study on the seismotectonic characters of the Zhangjiakou-Penglai fault zone. Seismol. Geol. 20 (2), 146–154 (in Chinese with an English abstract).
- Xu, M., Li, Y., Hou, H., Wang, C., Gao, R., Wang, H., et al., 2017. Structural characteristics of the Yilan-Yitong and Dunhua-Mishan faults as northern extensions of the Tancheng-Lujiang fault zone: New deep seismic reflection results. Tectonophysics 706–707, 35–45. https://doi.org/10.1016/j.tecto.2017.03.018.

- Xu, X., Ma, X., Deng, Q., 1993. Neotectonic activity along the Shanxi rift system, China. Tectonophysics 219, 305–325. https://doi.org/10.1016/0040-1951(93) 90180-R.
- Ye, H., Zhang, B., Mao, F., 1987. The Cenozoic tectonic evolution of the great North China: two types of rifting and crustal necking in the great North China and their tectonic implications. Tectonophysics 133 (3–4), 217–227. https://doi.org/ 10.1016/0040-1951(87)90265-4.
- Yin, A., Yu, X., Shen, Z.K., Liu-Zeng, J., 2014. A possible seismic gap and high earthquake hazard in the North China basin. Geology 43 (1), 19–22. https:// doi.org/10.1130/g35986.1.
- Zhang, P., Deng, Q., Zhang, G., Ma, J., Gan, W., Min, W., et al., 2003. Active tectonic blocks and strong earthquakes in the continent of China. Sci. China, Ser. D, Earth Sci. 46, 13–24. https://doi.org/10.1360/03dz0002.
- Zhang, Y., Ma, Y., Yang, N., Shi, W., Dong, S., 2003. Cenozoic extensional stress evolution in North China. J. Geodyn. 36 (5), 591–613. https://doi.org/10.1016/j.jog. 2003.08.001
- Zhang, Y.G., Zheng, W.J., Wang, Y.J., Zhang, D.L., Tian, Y.T., Wang, M., et al., 2018. Contemporary deformation of the North China plain from global positioning system data. Geophys. Res. Lett. 45 (4), 1851–1859. https://doi.org/10.1002/2017gl076599.
- Zhao, B., Huang, Y., Zhang, C., Wang, W., Tan, K., Du, R., 2015. Crustal deformation on the Chinese mainland during 1998–2014 based on GPS data. Geod. Geodyn. 6 (1), 7–15. https://doi.org/10.1016/j.geog.2014.12.006.
- Zhao, G., Sun, M., Wilde, S.A., Sanzhong, L., 2005. Late archean to paleoproterozoic evolution of the North China craton: key issues revisited. Precambrian Res. 136 (2), 177–202. https://doi.org/10.1016/j.precamres.2004.10.002.
- Zhao, X., Coe, R.S., 1987. Palaeomagnetic constraints on the collision and rotation of North and south China. Nature 327 (6118), 141–144. https://doi.org/10.1038/327141a0

- Zheng, G., Wang, H., Wright, T.J., Lou, Y., Zhang, R., Zhang, W., et al., 2017. Crustal deformation in the India-Eurasia collision zone from 25 years of GPS measurements. J. Geophys. Res., Solid Earth 122 (11), 9290–9312. https://doi.org/10.1002/2017jb014465.
- Zheng, Y.-F., Xiao, W.-J., Zhao, G., 2013. Introduction to tectonics of China. Gondwana Res. 23 (4), 1189–1206. https://doi.org/10.1016/j.gr.2012.10.001.
- Zhu, G., Hu, W., Song, L., Liu, B., 2015. Quaternary activity along the tan-Lu fault zone in the Bohai Bay, East China: evidence from seismic profiles. J. Asian Earth Sci. 114, 5–17. https://doi.org/10.1016/j.jseaes.2015.03.030.
- Zhu, G., Liu, G.S., Niu, M.L., Xie, C.L., Wang, Y.S., Xiang, B., 2007. Syn-collisional transform faulting of the Tan-Lu fault zone, East China. Int. J. Earth Sci. 98 (1), 135–155. https://doi.org/10.1007/s00531-007-0225-8.
- Zhu, G., Niu, M., Xie, C., Wang, Y., 2010. Sinistral to normal faulting along the Tan-Lu fault zone: evidence for geodynamic switching of the East China continental margin. J. Geol. 118 (3), 277–293. https://doi.org/10.1086/651540.
- Zhu, R., Xu, Y., 2019. The subduction of the West Pacific plate and the destruction of the North China craton. Sci. China Earth Sci. 62 (9), 1340–1350. https://doi.org/10.1007/s11430-018-9356-y.
- Zhu, R., Zhang, H., Zhu, G., Meng, Q., Fan, H., Yang, J., et al., 2017. Craton destruction and related resources. Int. J. Earth Sci. 106 (7), 2233–2257. https://doi.org/10.1007/s00531-016-1441-x.
- Zonenshain, L., Savostin, L., 1981. Geodynamics of the Baikal rift zone and plate tectonics of Asia. Tectonophysics 76 (1–2), 1–45. https://doi.org/10.1016/0040-1951(81)90251-1.